

From Voxel to Point: IoU-guided 3D Object Detection for Point Cloud with Voxel-to-Point Decoder

Jiale Li
 jialeli@zju.edu.cn
 Zhejiang University
 Hangzhou, China

Ling Shao
 ling.shao@ieee.org
 Inception Institute of Artificial Intelligence
 Abu Dhabi, United Arab Emirates

Hang Dai*
 hang.dai@mbzuai.ac.ae
 Mohamed bin Zayed University of Artificial Intelligence
 Abu Dhabi, United Arab Emirates

Yong Ding*
 dingy@vlsi.zju.edu.cn
 Zhejiang University
 Hangzhou, China

ABSTRACT

In this paper, we present an Intersection-over-Union (IoU) guided two-stage 3D object detector with a voxel-to-point decoder. To preserve the necessary information from all raw points and maintain the high box recall in voxel based Region Proposal Network (RPN), we propose a residual voxel-to-point decoder to extract the point features in addition to the map-view features from the voxel based RPN. We use a 3D Region of Interest (RoI) alignment to crop and align the features with the proposal boxes for accurately perceiving the object position. The RoI-Aligned features are finally aggregated with the corner geometry embeddings that can provide the potentially missing corner information in the box refinement stage. We propose a simple and efficient method to align the estimated IoUs to the refined proposal boxes as a more relevant localization confidence. The comprehensive experiments on KITTI and Waymo Open Dataset demonstrate that our method achieves significant improvements with novel architectures against the existing methods. The code is available on Github URL¹.

CCS CONCEPTS

• **Computing methodologies** → **Object detection; Scene understanding; Vision for robotics.**

KEYWORDS

object detection, 3D object, point clouds, segmentation

ACM Reference Format:

Jiale Li, Hang Dai, Ling Shao, and Yong Ding. 2021. From Voxel to Point: IoU-guided 3D Object Detection for Point Cloud with Voxel-to-Point Decoder. In *Proceedings of the 29th ACM International Conference on Multimedia (MM '21)*, October 20–24, 2021, Virtual Event, China. ACM, New York, NY, USA, 10 pages. <https://doi.org/10.1145/3474085.3475314>

*Corresponding authors.

¹<https://github.com/jialeli1/From-Voxel-to-Point>

Permission to make digital or hard copies of all or part of this work for personal or classroom use is granted without fee provided that copies are not made or distributed for profit or commercial advantage and that copies bear this notice and the full citation on the first page. Copyrights for components of this work owned by others than ACM must be honored. Abstracting with credit is permitted. To copy otherwise, or republish, to post on servers or to redistribute to lists, requires prior specific permission and/or a fee. Request permissions from permissions@acm.org.
 MM '21, October 20–24, 2021, Virtual Event, China

© 2021 Association for Computing Machinery.
 ACM ISBN 978-1-4503-8651-7/21/10...\$15.00
<https://doi.org/10.1145/3474085.3475314>

1 INTRODUCTION

Three dimensional object detector localizes objects with tight 3D bounding boxes. Compared with monocular and stereo image based approaches [5, 19, 26, 27, 41], LiDAR based methods are more robust in autonomous driving [8, 38]. Current 3D object detectors mainly represent the point cloud as raw points or voxels. Point-based methods [34, 46] argue that the raw points preserve the pose information of objects, which is crucial to accurate localization. Voxel-based methods [11, 45] voxelize the point cloud in a voxel encoder and project the voxel features onto Bird's Eye View (BEV) as the map-view features. The Region Proposal Network (RPN) built on the map-view features [33, 35] can achieve higher box recall than that built on the point features [34, 47].

The structure information of the objects are abstracted to the map-view features with downsampling in the voxel encoder [45], which results in the lose of the detailed pose information in the raw points. To avoid this and maintain the high box recall in the RPN stage, we propose a novel voxel-to-point decoder to extract the discriminative 3D point features from the raw points. The voxel-to-point decoder consists of stacked residual voxel-to-point decoding blocks with skip connections [32]. In each decoding block, we aggregate the features of the voxels that are surrounding the raw point as the voxel-to-point features. In the stacked decoding blocks, We use a residual learning [13] between the point features from the previous level and the current voxel-to-point features to extract enhanced point features that gradually become fine-grained through the hierarchical feature aggregation. A segmentation mask is used to supervise the point feature learning, which makes it sensitive to the foreground and the background information. We propose a 3D Region of Interest (RoI) alignment to align the point features and the map-view features with the proposal boxes for accurately perceiving the object position. Since the eight corners of the 3D bounding boxes do not always exist in the raw points, the RoI-Aligned features are finally aggregated with the corner geometry embeddings that provide the missing corner information.

The reasons why not use another point-based network like [23, 29, 30] to provide the point features starting from the raw points are as follows. In our method, we aggregate the features of the voxels that are in the K -nearest neighbors of the raw point as the voxel-to-point features. Each voxel has grouped the internal points together in the voxel encoder [50] for enlarging the receptive field [30], which is more informative than the raw point aggregation. The

voxel encoder is shared in both the map-view feature learning and the point feature learning, which is more computationally efficient.

In a two-stage object detector, the second stage takes the proposal boxes from the RPN stage as input to classify the foreground object proposals and predict the residuals to their ground truth for further box refinement [31]. The classification scores are typically used as the metric to rank the proposal boxes for removing the redundant boxes in the Non-Maximum Suppression (NMS) procedure. Since classification and localization are solved separately, the localization confidence is always absent in the object detection pipeline. The IoU is a natural criterion for localization accuracy as the ranking criterion in NMS. Inspired by [14, 47], we train a 3D IoU estimation branch that is parallel to other regression branches. However, there exists a misalignment between the estimated IoUs and the refined boxes in the existing methods. Since the estimated IoUs are regressed from RoI-Aligned features using the proposal boxes, the estimated IoUs are aligned to the proposal boxes, not the refined proposal boxes. Thus, the estimated IoUs from the proposal boxes cannot be used as the localization confidence for the refined proposal boxes in NMS for box de-redundancy.

A straightforward approach is to train the IoU estimation branch [14] using the actual IoUs of the refined boxes. However, there are two issues: i) Since the refined boxes are always one stage later than the proposal boxes, we cannot obtain the refined boxes in the training of the refinement stage. We need an additional stage to train a new IoU estimation branch for the refined boxes, which brings more network parameters and computational costs. ii) Although we can infer the box regression branch to refine the proposal boxes and compute the actual IoUs of the refined boxes for training a parallel IoU estimation branch, there raises another misalignment between the RoI-Aligned features and the IoU training labels. The IoUs of the refined box should be regressed from the RoI-Aligned features of the refined boxes other than that of the proposal boxes. With a well-trained parallel IoU estimation branch, we can resolve this misalignment simply and efficiently by updating the proposal boxes with the refined proposal boxes with one more inference stage. The second-time estimated IoUs are aligned to the refined proposal boxes and used as the localization confidence.

2 RELATED WORK

Grid-based 3D Object Detection. Grid-based methods convert the point clouds of unstructured data format to the regular grids like pixels and voxels for 2D or 3D convolutional processing. The early work MV3D [3] projects the points as pixels in an image of bird’s-eye view (BEV) for feature extraction and 3D bounding box proposal with efficient 2D CNN. The following works [15, 21] leverage the camera image features to compensate the BEV point cloud features with effective fusion strategies. Besides, VoxelNet [50] divides the points into small 3D voxels for 3D CNN and PointPillars [16] constructs the pseudo-images after voxelization. Due to the high computational cost caused by a large number of empty voxels, 3D sparse CNN [9, 10] is introduced for efficient computation by SECOND [45]. Based on [45], PartA2 [35] explores the object part locations for finer 3D structure information learning. Discretizing the points to grids with limited resolution brings computational efficiency, but it weakens the information interpretation.

Point-based 3D Object Detection. Point based methods take the raw point cloud as input, and apply PointNet++ [30] or Graph Neural Networks (GNN) [43] for point-wise feature learning and object detection. PointNet++ based methods [17, 34, 47] maintain the resolution of the point cloud, while 3DSSD [46] downsamples a relatively balanced number of foreground and background points, and discards the upsampling process. Different from the hierarchical feature aggregation, Point-GNN [36] utilize GNN to iteratively update the features of the entire point cloud. Precise point coordinates are directly embedded into features, but it is not efficient in point sampling and grouping with a low box recall.

Voxel-Point based 3D Object Detection. The voxel-point based methods [18, 33, 47] use both representations. PointsPool [47] voxelizes the point cloud around the object proposal to encode the empty and non-empty regions for compact proposal-wise feature learning. PV-RCNN [33] proposes a Voxel Set Abstraction operation to aggregate the voxel-wise features in the backbone to some sampled keypoints. Then the keypoints are utilized for the bounding box refinement. Similarly, SA-SSD [11] converts the voxel-wise backbone features back to the point-wise features only for auxiliary supervision, which is not an effective way to exploit the point-wise features with accurate position information.

Ours VS. PV-RCNN. In PV-RCNN [33], a set of keypoints (2,048 points) is sampled to roughly represent the entire point cloud scene (~20K points), while only a small number of sampled keypoints distributed near the foreground objects can be used for the box refinement. To preserve more object details, we maintain the full point features of the raw points with our voxel-to-point decoder for the detection refinement with significant improvement, especially for the distant objects with much more sparse points. In PV-RCNN, voxel features of different levels are simply concatenated to each sampled point, while our decoder gradually enhances the point features through the hierarchical feature aggregation with residual learning. Unlike PV-RCNN that aligns the map-view feature to the several sampled keypoints, we align the map-view features to the evenly distributed grid points inside the object to focus more on the object region as shown in Figure 3 (b). Besides, the absolute coordinates are used in the pooling operation of PV-RCNN, which is not robust to rigid transformations. Instead, we normalize both the coordinates of the raw points and grid points as the relative coordinates that are centered on the object proposal and aligned to the object proposal’s orientation.

3 METHOD

This section presents our IoU-guided 3D object detection with voxel-to-point decoder. We first explicitly define the point cloud 3D object detection task in Section 3.1. Then the overall network structure is introduced in Section 3.2. The voxel encoder and RPN are presented in Section 3.3. In Section 3.4 and 3.5, we describe a residual voxel-to-point decoder and an IoU-guided detection refinement in detail. The loss functions are presented in Section 3.6.

3.1 Problem Definition

The network takes one frame of the point cloud as input to localize the objects in the form of 3D boxes with localization confidence. The 3D box is represented as the 3D center point (o_x, o_y, o_z) , size

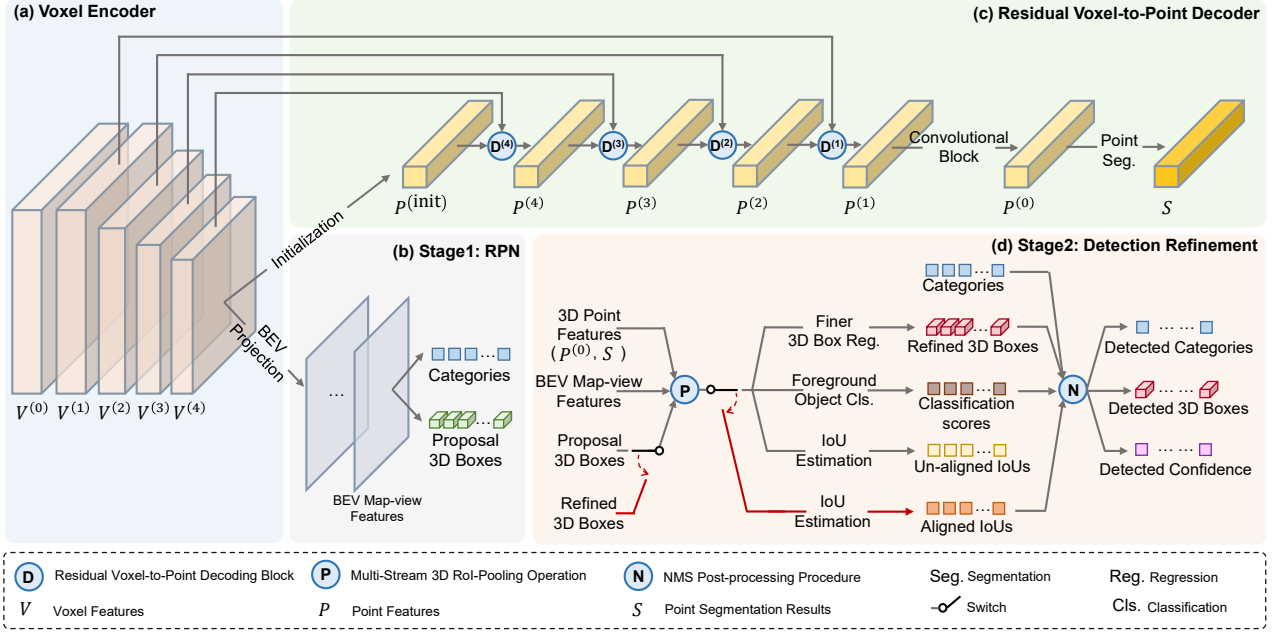


Figure 1: The framework of the proposed 3D object detection network. The red arrows represent the second-time inference by switching from the proposal boxes to the refined boxes for the 3D IoU alignment. The figure is best viewed in color.

(l, w, h), and rotation angle θ_{rot} around Z-axis. The localization confidence between 0 and 1 is also estimated by the network. Let $\{p_i = (x_i, y_i, z_i) : i = 1, \dots, N\}$ be the coordinates of point cloud in the range of $[X_{\min}, X_{\max}], [Y_{\min}, Y_{\max}], [Z_{\min}, Z_{\max}]$.

3.2 Overall Network Architecture

Figure 1 describes the overall network with four components: (a) the voxel encoder that extracts 3D voxel features; (b) an RPN where 3D voxel features are projected onto BEV as the map-view features for the object classification, and the localization of the coarse 3D box as the proposal box; (c) the voxel-to-point decoder that extracts the fine-grained point features from the voxel features; (d) the IoU-guided detection refinement stage for refining the proposal boxes and estimating the localization confidence.

3.3 Voxel Encoder and RPN

The point cloud is voxelized by a quantization step $d = [d_x, d_y, d_z]$ as $\{\bar{p}_i = (\lfloor \frac{x_i - X_{\min}}{d_x} \rfloor, \lfloor \frac{y_i - Y_{\min}}{d_y} \rfloor, \lfloor \frac{z_i - Z_{\min}}{d_z} \rfloor) : i = 1, \dots, N\}$, then re-organized into the sparse voxel tensor. The voxel index is the unique integer \bar{p}_i and the voxel feature is initialized as the mean of the 3D coordinates and reflection intensities of all the points within the voxel [33, 35]. The voxel encoder takes the sparse voxel tensor as input for learning the multi-level voxel features V in sparse convolution blocks [10] with downsampling stride s . Then the output voxel features are projected to BEV for generating the dense object proposals. We adopt the voxel based networks [45, 50] and the regression heads in [45] as our voxel encoder and RPN.

3.4 Residual Voxel-to-Point Decoder

We propose a residual voxel-to-point decoder to provide the full point features with sufficient object positional information. As

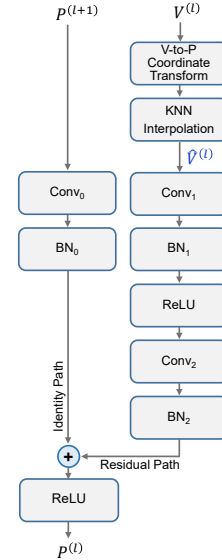


Figure 2: Residual voxel-to-point decoding block with Convolution (Conv), Batch Normalization (BN), and ReLU.

shown in Figure 1 (c), we hierarchically aggregate the multi-level voxel features V through the skip connections [30, 32] and the stacked residual voxel-to-point decoding blocks \mathcal{D} . In the block $\mathcal{D}^{(l)}$ at level l , the current point features $P^{(l)}$ is updated from previous point features $P^{(l+1)}$ and the lateral voxel features $V^{(l)}$ in the residual block [13].

Figure 2 presents the decoding block $\mathcal{D}^{(l)}$. For each point, considering the neighbors is crucial to the point feature learning

[30] for enlarging the receptive field. The features of the voxels that are in the K -Nearest neighbors of the raw point can be aggregated as the voxel-to-point features. The point features $P^{(l+1)}$ on the previous level are used as the identity information while the newly aggregated voxel-to-point features are used as residual information for the enhanced point features $P^{(l)}$. The insight of the design is to conduct the residual learning between the point features from the previous level and the voxel-to-point features for fine-grained feature extraction. We transform the integer voxel index $(v_x^{(l)}, v_y^{(l)}, v_z^{(l)})$ back to the raw point coordinate system by representing voxel as point with floating-point $p^{(l)} = (x^{(l)}, y^{(l)}, z^{(l)})$ on the voxel center according to the downsampling stride $s^{(l)}$, initial quantization step as $d = [d_x, d_y, d_z]$, and the point cloud boundaries. The voxel-to-point coordinate transformation can be formulated as:

$$\begin{cases} x^{(l)} = (v_x^{(l)} + 0.5) \times d_x \times s + X_{\min}, \\ y^{(l)} = (v_y^{(l)} + 0.5) \times d_y \times s + Y_{\min}, \\ z^{(l)} = (v_z^{(l)} + 0.5) \times d_z \times s + Z_{\min}, \end{cases} \quad (1)$$

where the offset 0.5 is to centralize the voxel index as the voxel center point. Then we obtain a intermediate point cloud as $\{(p_i^{(l)}, V_i^{(l)}) : i = 1, \dots, N^{(l)}\}$ with points $p^{(l)}$ and the corresponding sparse features $V^{(l)}$ from the voxel encoder. To enhance the previous point features $P^{(l+1)}$ with the intermediate point cloud, we upsample it to be aligned with the resolution of raw points by the interpolation-based feature propagation [30]. The interpolation is implemented as the inverse distance weighted average w among the K -Nearest Neighbors (KNN) in $p^{(l)}$ as:

$$\hat{V}_i^{(l)} = \sum_k \frac{w_k(p_i) V_k^{(l)}}{\sum_k w_k(p_i)}, i = 1, \dots, N, \quad (2)$$

$$w_k(p_i) = \frac{1}{\|p_k^{(l)} - p_i\|}. \quad (3)$$

The decoding block $\mathcal{D}^{(l)}$ finally combines the previous point features $P^{(l+1)}$ and the voxel-to-point feature $\hat{V}^{(l)}$ in a manner of residual learning for output $P^{(l)}$. Each voxel has grouped the internal points together in the voxel encoder. From $V^{(4)}$ to $V^{(1)}$, the number of voxels gradually increases. Since the multi-level voxel features are hierarchically aggregated with the residual learning of the point features, the final point features $P^{(1)}$ are gradually enhanced. In the first decoding block $\mathcal{D}^{(4)}$, we can initialize the point feature $P^{(\text{init})}$ to be adapted from the voxel feature $V^{(4)}$ using the interpolation-based feature propagation. The K is set as 3 for computational efficiency.

To explicitly guide the residual voxel-to-point decoder to focus on the 3D structure information of the foreground objects, we use an auxiliary segmentation task for a supervised semantic point feature learning. The last decoding block is followed by a 1-D convolutional block for feature embedding and another one for the auxiliary point-wise semantic segmentation output S . The point-wise labels can be generated by determining whether the point is within the annotated box or not. Since the foreground points on the object are less than the background points, especially in the large-scale outdoor scenes,

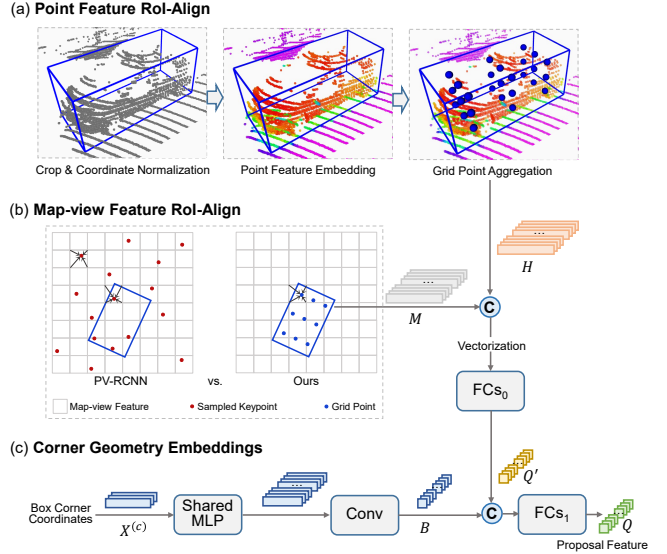


Figure 3: Multi-stream RoI pooling. Multi-Layer Perceptron (MLP), Convolution (Conv), Fully Connected layers (FCs).

we adopt the focal loss [22] with the default settings to deal with such an imbalance.

3.5 IoU-guided Detection Refinement

3.5.1 Multi-stream 3D RoI Pooling. Point Feature RoI-Align.

The point feature RoI-Align operation is performed to accurately perceive the object location with $P^{(0)}$ and S provided by our voxel-to-point decoder. As shown in Figure 3 (a), the 3D points around a proposal are cropped by the expanded proposal box as the point-stream RoI feature. We add a margin d_{size} to the size of the box to increase the tolerance of the proposal localization for including more surrounding necessary information of the object. The cropped point cloud is normalized to the relative coordinate system centered on the proposal center and aligned to the proposal rotation angle, which makes it more robust to the rigid transformations [34]. Next, we aggregate the point-wise local features with the semantic mask S . For each point, the relative coordinates \tilde{p}_i represent the pose information, the depth \tilde{D}_i provides the distance information, and the semantic mask \tilde{S}_i makes it sensitive to the foreground and the background information. Note that the symbol “ \sim ” indicates the relative coordinate system in the cropped point cloud. The low-dimensional local features $\{(\tilde{p}_i, \tilde{D}_i, \tilde{S}_i)\}$ are concatenated together and transformed as the expressive high-dimensional feature representation \tilde{P}'_i with a Multi-Layer Perceptron (MLP). The point-wise feature is obtained from \tilde{P}' and $P^{(0)}$:

$$\tilde{P}'_i = \text{MLP}_1([\tilde{p}_i \odot \tilde{D}_i \odot \tilde{S}_i]), \quad (4)$$

$$\tilde{P}_i = \text{MLP}_2([\tilde{P}'_i \odot P^{(0)}_i]), \quad (5)$$

where “ \odot ” indicates the concatenation. In the third step, we use the grid point aggregation [33]. The proposal box is divided into $N_G = N_g \times N_g \times N_g$ regularly distributed grid points. Given a grid point \hat{g}_n , we group a set of K_1 neighboring points within radius r

for feature aggregation along with set abstraction [30]:

$$H_n = \max_k \{ \text{MLP}_3 [(\tilde{p}_k - \tilde{g}_n) \odot \tilde{p}_k] \} \quad (6)$$

where $\|\tilde{p}_k - \tilde{g}_n\| < r$. The C_h -dimensional RoI-Aligned point feature can be formulated with all the grid points:

$$H = [H_1, \dots, H_n, \dots, H_{N_G}] \in \mathbb{R}^{C_h \times N_G}. \quad (7)$$

We set the multiple group radii in the set abstraction for multi-scale information aggregation [30], and determine the box size margin d_{size} as the group radius.

Map-view Feature RoI-Align. Since the receptive field of the map-view feature in RPN increases in the hierarchical voxel encoder blocks, the map-view feature discards the details of objects but retains the structural information of objects. Thus, we use the grid points instead of the sampled keypoints in [33] to extract the compact map-view feature in the regions of objects. The local grid points \tilde{g} is first transformed back to the global coordinate system in the raw point cloud. Then we project them onto BEV. The coordinates $(g_x^{(bev)}, g_y^{(bev)})$ of the projected grid points on the map-view feature can be calculated by grid point global coordinates g , down-sample stride $s^{(bev)}$ of map-view feature, quantization d , and point cloud boundary as:

$$\begin{cases} g_x^{(bev)} = (g_x - X_{\min}) / (d_x \times s^{(bev)}), \\ g_y^{(bev)} = (g_y - Y_{\min}) / (d_y \times s^{(bev)}). \end{cases} \quad (8)$$

To avoid the quantization errors as introduced in [12, 31], we directly keep the floating-point coordinates $g^{(bev)}$ instead of rounding them. Given a projected grid point $g_n^{(bev)}$, we use the bilinear interpolation to compute its map-view feature M_n from its four nearest integer neighbors, which is clearly illustrated in Figure 3 (b). The C_m -dimensional map-view RoI feature M aligned by N_G grid points can be formulated as:

$$M = [M_1, \dots, M_n, \dots, M_{N_G}] \in \mathbb{R}^{C_m \times N_G}. \quad (9)$$

Corner Geometry Embeddings. The eight corners of the box are not usually included in the raw points, but they are closely related to the localization accuracy. Most methods only focus on the RoI features and ignore the geometry information of the boxes. The Corner Geometry Embeddings (CGEs) include the box geometry information in addition to the RoI features. As illustrated in Figure 3 (c), the eight corners' coordinates $X^{(c)} \in \mathbb{R}^{3 \times 8}$ are projected into a C'_b -dimensional space, ensuring that the low-dimensional coordinates of corners are not overwhelmed by the high-dimensional RoI features. Secondly, a 1-D convolution with kernel $\theta \in \mathbb{R}^{C_b \times C'_b \times 8}$ is applied to the eight corners for the final CGEs $B \in \mathbb{R}^{C_b \times 1}$.

Multi-stream Feature Aggregation. As shown in Figure 3, the RoI-Aligned point feature H and map-view feature M are first concatenated together, then vectorized to be fused as Q' in a set of Fully Connected layers (FCs). Another set of FCs is used to transform the concatenation of the CGEs B and Q' as the final proposal feature Q for the detection branches, including a classification, a box regression, and an IoU estimation branch. All the three parallel branches are implemented in the same structure, consisting of a set of FCs for feature embedding and another fully

connected layer with a different number of neurons adapting to the dimension of the output.

3.5.2 3D IoU Alignment. The IoU misalignment is caused by the proposal box refinement. Since the estimated IoUs are regressed from RoI-Aligned features using the proposal boxes, they are aligned to the proposal boxes, not the refined proposal boxes. The estimated IoUs from the proposal boxes cannot be used as the localization confidence for the refined proposal boxes in NMS. To align the estimated IoUs to the refined boxes, we replace the proposal boxes in the 3D RoI pooling with the refined proposal boxes in one more inference stage without training. Then the computed IoUs are aligned to the refined proposal boxes and used as the localization confidence for the refined proposal boxes de-redundancy in NMS.

3.6 Loss Function

Our network is optimized by a multi-task loss $\mathcal{L}_{\text{total}}$ as:

$$\mathcal{L}_{\text{total}} = \alpha_1 \mathcal{L}_{\text{rpn}} + \alpha_2 \mathcal{L}_{\text{seg}} + \alpha_3 \mathcal{L}_{\text{refine}}, \quad (10)$$

where the coefficients α_1 , α_2 , and α_3 are set to 1.0, 4.0, and 1.0 to balance the RPN loss \mathcal{L}_{rpn} in [45], the point segmentation loss \mathcal{L}_{seg} to supervise the semantic point feature learning, and the detection refinement loss $\mathcal{L}_{\text{refine}}$, respectively. The $\mathcal{L}_{\text{refine}}$ can be further formulated as:

$$\mathcal{L}_{\text{refine}} = \mathcal{L}_{\text{cls}} + \mathcal{L}_{\text{reg}} + \mathcal{L}_{\text{iou}}. \quad (11)$$

The classification loss \mathcal{L}_{cls} is computed using the binary cross entropy loss. The box regression loss \mathcal{L}_{reg} and the IoU estimation loss \mathcal{L}_{iou} are both computed using the smooth-L1 loss on the N_{reg} proposals with $\text{IoU} \geq \theta_{\text{reg}}$ in a manner as:

$$\mathcal{L} = \frac{1}{N_{\text{reg}}} \sum_i [\text{IoU}_i \geq \theta_{\text{reg}}] \mathcal{L}_{\text{smooth-L1}}(a_i, \hat{a}_i), \quad (12)$$

where a_i and \hat{a}_i denote the target and prediction of specific item (*i.e.*, IoU and the residuals of center coordinates, size, orientation) for the i -th proposal. The Iverson bracket indicator function $[\text{IoU}_i \geq \theta_{\text{reg}}]$ sets as 1 when $\text{IoU}_i \geq \theta_{\text{reg}}$, otherwise, it sets as 0.

4 EXPERIMENTS

4.1 Datasets

KITTI Dataset. The KITTI [8] is one of the most widely used 3D object detection datasets for autonomous driving. It contains 7481 training samples and 7518 testing samples, and annotates objects in the camera Field of Vision (FOV). We follow the common practice to divide the training samples as *train* split set (3712 samples) and the *val* split set (3769 samples) [3, 33, 45]. For submitting the results on the *test* set to the online benchmark, the training samples are randomly divided into two sets at a ratio of 4 : 1 for training and validation following [33, 47].

Waymo Open Dataset. The newly released Waymo Open Dataset (WOD) [38] is currently the largest public dataset for autonomous driving, including $\sim 158\text{K}$ point cloud training samples and $\sim 40\text{K}$ point cloud validation samples. Different from KITTI, the WOD provides object annotations in the full 360° fields. To further verify the effectiveness of our method, we also evaluate the performance of our method on the more challenging dataset WOD.

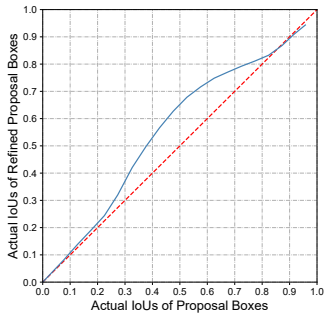


Figure 4: IoU curve of proposal boxes and refined boxes.

Table 1: Detection performance comparison of the architectures without and with detection refinement. The classification score is used as the detection confidence following PV-RCNN[33] to exclude the effects of IoU alignment.

Detection Refinement	3D AP		
	Easy	Mod.	Hard
×	88.98	80.85	78.79
√	92.69	85.38	83.23

4.2 Implementation Details

Voxelization. Since the KITTI only provides the annotations in FOV, we set the quantization step d as (0.05, 0.05, 0.1) meters to voxelize point cloud within the range of $[0, 70.4]$, $[-40, 40]$, $[-3, 1]$ meters in X , Y , Z -axis. For WOD, the range of point cloud is $[-75.2, 75.2]$, $[-75.2, 75.2]$, $[-2, 4]$ meters for X , Y , Z -axis, and the quantization step d is (0.1, 0.1, 0.15) meters.

Network Architectures. The architecture of our voxel encoder follows the design in [33, 45]. It downsamples the voxel volumes with $1\times$, $2\times$, $4\times$, $8\times$ while it increases the feature dimension as 16, 32, 64, 128. The RPN head is adopted from the [45] for region proposal. The residual voxel-to-point decoder gradually aggregates the different number of voxels from the different voxel feature levels to the raw point clouds with the output feature dimension as 256, 192, 160, 128 and 128 for $P^{(4)}$, $P^{(3)}$, $P^{(2)}$, $P^{(1)}$ and $P^{(0)}$, respectively. For each proposal in the detection refinement stage, $N_G = 6 \times 6 \times 6$ grid points are generated to aggregate the cropped point clouds with multiple group radii (0.8, 1.6) meters. The feature dimension C_h , C_m and C_b are set as 128 for RoI-Aligned point features, RoI-Aligned map-view features and corner geometry embeddings.

Training. Our model is trained from scratch in an end-to-end manner with the AdamW optimizer [25] and one-cycle policy [37] with LR 0.01, division factor 10, momentum ranges from 0.95 to 0.85, weight decay 0.01. A batch of 8 or 48 random point cloud samples is trained on 4 or 16 Tesla V100 GPUs with 80 or 30 epochs for KITTI and WOD, respectively. For the detection refinement stage, we sample 128 proposals from the RPN as the training samples. The foreground IoU threshold θ_H is set as 0.75, the background IoU threshold θ_L is set as 0.25 for classification branch. The threshold θ_{reg} mentioned in Equation 12 is empirically set as 0.55 to select approximately half of the sampled proposals for box regression and IoU estimation training, which follows [33, 34, 47]. To avoid overfitting, we employ four commonly used data augmentation strategies: ground truth sampling [45], random flipping along the

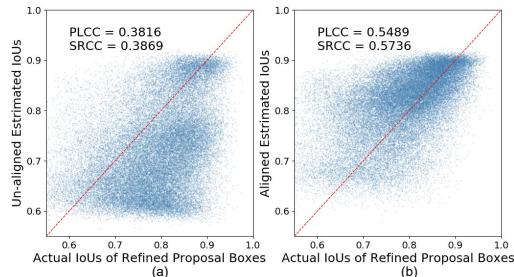


Figure 5: Correlation between the estimated IoUs and the actual IoUs. Pearson’s Linear Correlation Coefficient (PLCC) and Spearman’s Rank order Correlation Coefficient (SRCC) describe the linear and the order correlation. Higher, better.

Table 2: Comparison of different localization confidences.

Tag	Localization Confidence	3D AP		
		Easy	Mod.	Hard
A	Classification score	92.69	85.38	83.23
B	Un-aligned IoUs	92.51	84.95	82.89
C	Aligned IoUs	93.09	85.54	83.38
D	Aligned IoUs×Classification score	93.00	85.61	83.43

X -axis, global scaling with a random scaling factor in $[0.95, 1.05]$, global rotation around the Z -axis with a random angle in $[-\frac{\pi}{4}, \frac{\pi}{4}]$.

Inference. We perform the NMS from the RPN proposals with IoU threshold 0.85 to take the top-100 proposals as the input of the detection refinement stage. After refining the top-100 proposals, we align the estimated IoUs to the refined boxes.

4.3 Ablation Study

We conduct an extensive ablation study to analyze each component in our method. All models are trained with the same settings on the KITTI *train* split set and evaluated with 3D average precision (AP) from 40 recall positions for the car class on the KITTI *val* split set [11, 33, 46]. The best results are in bold. Objects are marked as three detection difficulties (easy, moderate, and hard) by KITTI, depending on their size, occlusion level, and truncation of 3D boxes.

Detection Refinement Stage. Table 1 shows that the detection refinement stage can significantly improve the performance. We plot the actual IoU changes of the proposal boxes and the refined proposal boxes in Figure 4. It shows that the actual IoUs of the refined proposal boxes become higher than those of the proposal boxes, indicating the improvements in localization accuracy.

3D IoU Alignment. We use four sets of localization confidence as shown in Table 2. When we directly use the un-aligned IoUs estimated from the proposal boxes as the localization confidence, the localization accuracy is worse than that based on the classification score. To address the IoU misalignment, we do one more inference to estimate the IoUs from the RoI features aligned with the refined proposal boxes. The aligned IoUs guided NMS achieves higher 3D AP than the first two in Table 2. As shown in Figure 5, compared with the un-aligned IoUs, the aligned IoUs become more correlated to the actual IoUs of the refined proposal boxes. Besides, when we

Table 3: Effects of each feature stream in 3D RoI-Pooling. Point, Map, and CGEs denote the RoI-Aligned point features, the RoI-Aligned map-view features, and the corner geometry embeddings.

Point	Map	CGEs	3D AP		
			Easy	Mod.	Hard
✓	✓	✓	93.00	85.61	83.43
×	✓	✓	92.38	82.88	80.24
✓	×	✓	92.78	85.32	83.15
✓	✓	×	92.91	85.41	83.21

Table 4: Performance comparison of the point feature learning with and without segmentation guidance.

Segmentation Supervision	3D AP		
	Easy	Mod.	Hard
×	92.79	85.34	83.10
✓	93.00	85.61	83.43

multiply the aligned IoUs and the classification score following STD [47], the detection performance can be further improved.

3D RoI Pooling. Table 3 shows the effectiveness of each individual feature stream. When the point features are removed, the detection performance drops significantly, which implies that the fine-grained point features provide additional information to improve the localization accuracy. For the moderate and hard objects with much more sparse points, the 3D AP drops by 2.73% and 3.19%. As shown in the last two rows of Table 3, the map-view features and the corner geometry embeddings also contribute to the performance gains by providing the object structure information and the box corner information. As we mentioned, the map-view feature loses the detailed pose information that is preserved in the points. Thus, the point features contribute more than the map-view features to the performance improvement.

Supervised Point Feature Learning. We train a model with our best model structure but learning point features in an unsupervised manner. Table 4 shows that the point segmentation supervision brings performance improvements of 0.21%, 0.27%, and 0.33% on 3D AP, indicating that the semantic information is useful in the point feature learning.

4.4 Results on KITTI Dataset

Evaluation Metric. We evaluate our method on the KITTI *test* set following the common practice to report the 3D AP calculated from 40 recall positions. The official benchmark sets the IoU thresholds for cars, cyclists, and pedestrians as 0.7, 0.5, and 0.5, respectively.

We report the 3D AP on the KITTI *test* set in Table 5 and Table 6. Table 5 shows the performance comparison on the commonly used car class. Our method that only uses the point cloud from LiDAR outperforms both the LiDAR + Camera based and the LiDAR only based existing methods, especially on the challenging moderate and hard objects with much more sparse points. Compared with PV-RCNN [33], our method increases by 0.15% and 0.55% on the moderate and hard objects. Note that the performance on the

Table 5: Performance comparison on car class of the KITTI *test* set. The top-2 results are in bold. “L” and “C” indicate the LiDAR and camera, respectively.

Method	Modality	3D AP		
		Easy	Mod.	Hard
MV3D[3]	L+C	74.97	63.63	54.00
AVOD[15]	L+C	83.07	71.76	65.73
Conti-Fuse[21]	L+C	83.68	68.78	61.67
F-PointNet[28]	L+C	82.19	69.79	60.59
UberATG-MMF[20]	L+C	88.40	77.43	70.22
PointPainting[39]	L+C	82.11	71.70	67.08
PI-RCNN[44]	L+C	84.37	74.82	70.03
VoxelNet[50]	L	77.47	65.11	57.73
SECOND[45]	L	83.34	72.55	65.82
PointPillars[16]	L	82.58	74.31	68.99
PointRCNN[34]	L	86.96	75.64	70.70
Fast PointRCNN[4]	L	85.29	77.40	70.24
STD[47]	L	87.95	79.71	75.09
TANet[24]	L	84.39	75.94	68.82
HotSpotNet[2]	L	87.60	78.31	73.34
Part-A2[35]	L	87.81	78.49	73.51
Associate-3Ddet[6]	L	85.99	77.40	70.53
SERCNN[48]	L	87.74	78.96	74.30
Point-GNN[36]	L	88.33	79.47	72.29
3DSSD[46]	L	88.36	79.57	74.55
PV-RCNN[33]	L	90.25	81.43	76.82
Ours	L	88.53	81.58	77.37

moderate difficulty is used as the ranking criterion in the official KITTI leaderboard. Table 6 shows the performance comparison between our method and other methods on the KITTI *test* set for cyclist and pedestrian classes, respectively. Our method also achieves state-of-the-art performance against the existing methods. The qualitative results are shown at the top of Figure 6.

4.5 Results on Waymo Open Dataset

Evaluation Metric. The WOD official evaluation toolkit provides two difficulty levels: LEVEL_1 for boxes with more than five LiDAR points, and LEVEL_2 for boxes with at least one LiDAR point. The true positive IoU threshold is also set to 0.7.

To show the detection performance in the large-scale point cloud scene that includes more object instances in the full 360° fields, we evaluate our method on both LEVEL_1 and LEVEL_2 of the newly released WOD with 3D AP and BEV AP, respectively. Table 7 shows that our method consistently outperforms all the other methods with a significant improvement across all the metrics. The detection difficulty generally increases as the object getting far away from the LiDAR sensor due to the fewer points that can be captured. The performance of our method on LEVEL_1 and LEVEL_2 improves much more significantly along with the distance. Our method demonstrates a more significant improvement on the large-scale point cloud scenes in WOD. Unlike the sparse point feature extraction in PV-RCNN, the proposed voxel-to-point

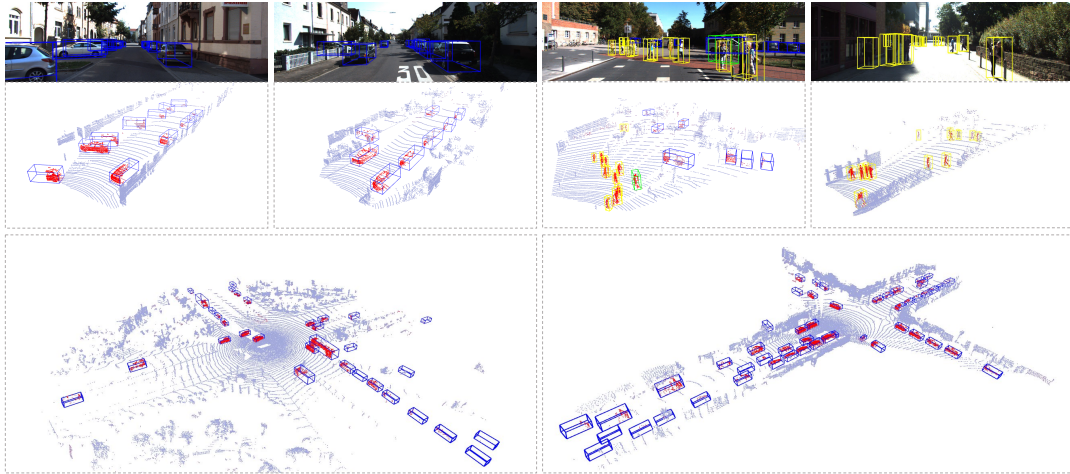


Figure 6: Qualitative results on KITTI (FOV) and Waymo (360°). Detected cars, cyclists, and pedestrians with blue, green, and yellow boxes, respectively. The color in point cloud shows segmentation results. Foreground in red. Background in gray.

Table 6: Performance comparison for the classes of cyclist and pedestrian on the KITTI *test* set by submitting to the official test server. The top-2 results are in bold.

Method	Cyclist			Pedestrian		
	Easy	Mod.	Hard	Easy	Mod.	Hard
AVOD-FPN[15]	63.76	50.55	44.93	50.46	42.27	39.04
BirdNet+[1]	67.38	47.72	42.89	37.99	31.46	29.46
SCNet[42]	67.98	50.79	45.15	47.83	38.66	35.70
F-PointNet[28]	72.27	56.12	49.01	50.53	42.15	38.08
PointRCNN[34]	74.96	58.82	52.53	47.98	39.37	36.01
PointPillars[16]	77.10	58.65	51.92	51.45	41.92	38.89
STD[47]	78.69	61.59	55.30	53.29	42.47	38.35
PointPainting[39]	77.63	63.18	55.89	50.32	40.97	37.87
SemanticVoxels[7]	N/A	N/A	N/A	50.90	42.19	39.52
PV-RCNN[33]	78.60	63.71	57.65	N/A	N/A	N/A
Ours	81.49	63.41	56.40	51.80	43.28	40.71

decoder enables the effective extraction of the fine-grained point features for all raw points in a residual learning manner, which is the key to the performance gains when the model is assembled with the detection refinement as shown in the ablation study. The qualitative results are shown at the bottom of Figure 6.

5 CONCLUSION

We present an IoU-guided two-stage 3D object detector with a voxel-to-point decoder. We use the voxel-to-point decoder to effectively extract the fine-grained point features, which is crucial to the performance gains in our two-stage detector. The proposed 3D RoI pooling is effective in refining the proposal boxes and estimating the IoUs. We use a simple and efficient method for aligning the estimated IoUs to the refined proposal boxes, thereby further improving the localization accuracy. Experimental results on KITTI and Waymo Open Dataset demonstrate that our method

Table 7: Performance on the Waymo Open Dataset validation for car detection. The top-1 results are in bold.

Difficulty	Method	overall	[0, 30)m	[30, 50)m	[50, Inf)m
LEVEL_1	3D AP				
	PointPillars[16]	56.62	81.01	51.75	27.94
	MVF[49]	62.93	86.30	60.02	36.02
	Pillar-OD[40]	69.80	88.53	66.50	42.93
	PV-RCNN[33]	70.30	91.92	69.21	42.17
	Ours	77.24	93.23	76.21	55.79
	<i>Improvement</i>	+6.94	+1.31	+7.00	+12.86
	BEV AP				
	PointPillars[16]	75.57	92.10	74.06	55.47
	MVF[49]	80.40	93.59	79.21	63.09
	Pillar-OD[40]	87.11	95.78	84.74	72.12
	PV-RCNN[33]	82.96	97.35	82.99	64.97
Ours	88.93	98.05	88.25	79.19	
<i>Improvement</i>	+1.82	+0.70	+3.51	+7.07	
LEVEL_2	3D AP				
	PV-RCNN[33]	65.36	91.58	65.13	36.46
	Ours	69.77	92.53	70.09	43.96
	<i>Improvement</i>	+4.41	+0.95	+4.96	+7.50
	BEV AP				
	PV-RCNN[33]	77.45	94.64	80.39	55.39
Ours	82.18	97.48	82.51	64.86	
<i>Improvement</i>	+4.73	+2.84	+2.12	+9.47	

outperforms state-of-the-art methods, and each component in our method is effective with performance gains.

ACKNOWLEDGMENTS

This work was supported by the National Key Research and Development Program of China under Grant 2018YFE0183900.

REFERENCES

- [1] Alejandro Barrera, Carlos Guindel, Jorge Beltrán, and Fernando García. 2020. BirdNet+: End-to-End 3D Object Detection in LiDAR Bird's Eye View. In *23rd IEEE International Conference on Intelligent Transportation Systems (ITSC)*. 1–6.
- [2] Qi Chen, Lin Sun, Zhixin Wang, Kui Jia, and Alan Yuille. 2020. Object as Hotspots: An Anchor-Free 3D Object Detection Approach via Firing of Hotspots. In *European Conference on Computer Vision (ECCV)*. 68–84.
- [3] Xiaozhi Chen, Huimin Ma, Ji Wan, Bo Li, and Tian Xia. 2017. Multi-view 3D Object Detection Network for Autonomous Driving. In *2017 IEEE Conference on Computer Vision and Pattern Recognition (CVPR)*. 6526–6534.
- [4] Yilun Chen, Shu Liu, Xiaoyong Shen, and Jiaya Jia. 2019. Fast Point R-CNN. In *2019 IEEE/CVF International Conference on Computer Vision (ICCV)*. 9774–9783.
- [5] Hang Dai, Shujie Luo, Yong Ding, and Ling Shao. 2020. Commands for autonomous vehicles by progressively stacking visual-linguistic representations. In *European Conference on Computer Vision (ECCV)*. Springer, 27–32.
- [6] Liang Du, Xiaoqing Ye, Xiao Tan, Jianfeng Feng, Zhenbo Xu, Errui Ding, and Shilei Wen. 2020. Associate-3Ddet: Perceptual-to-Conceptual Association for 3D Point Cloud Object Detection. In *2020 IEEE/CVF Conference on Computer Vision and Pattern Recognition (CVPR)*. 13326–13335.
- [7] Juncong Fei, Wenbo Chen, Philipp Heidenreich, Sascha Wirges, and Christoph Stiller. 2020. SemanticVoxels: Sequential Fusion for 3D Pedestrian Detection using LiDAR Point Cloud and Semantic Segmentation. In *IEEE International Conference on Multisensor Fusion and Integration for Intelligent Systems*. 185–190.
- [8] Andreas Geiger, Philip Lenz, and Raquel Urtasun. 2012. Are We Ready for Autonomous Driving? The KITTI Vision Benchmark Suite. In *2012 IEEE Conference on Computer Vision and Pattern Recognition, Providence (CVPR)*. 3354–3361.
- [9] Ben Graham. 2015. Sparse 3D Convolutional Neural Networks. In *2015 British Machine Vision Conference (BMVC)*. 150.1–150.9.
- [10] Benjamin Graham, Martin Engelcke, and Laurens van der Maaten. 2018. 3D Semantic Segmentation With Submanifold Sparse Convolutional Networks. In *2018 IEEE/CVF Conference on Computer Vision and Pattern Recognition (CVPR)*. 9224–9232.
- [11] Chenhang He, Hui Zeng, Jianqiang Huang, Xian-Sheng Hua, and Lei Zhang. 2020. Structure Aware Single-Stage 3D Object Detection From Point Cloud. In *2020 IEEE/CVF Conference on Computer Vision and Pattern Recognition (CVPR)*. 11870–11879.
- [12] Kaiming He, Georgia Gkioxari, Piotr Dollár, and Ross B. Girshick. 2017. Mask R-CNN. In *2017 IEEE International Conference on Computer Vision (ICCV)*. 2980–2988.
- [13] Kaiming He, Xiangyu Zhang, Shaoqing Ren, and Jian Sun. 2016. Deep Residual Learning for Image Recognition. In *2016 IEEE Conference on Computer Vision and Pattern Recognition (CVPR)*. 770–778.
- [14] Borui Jiang, Ruixuan Luo, Jiayuan Mao, Tete Xiao, and Yuning Jiang. 2018. Acquisition of Localization Confidence for Accurate Object Detection. In *European Conference on Computer Vision (ECCV)*. 784–799.
- [15] Jason Ku, Melissa Mozifian, Jungwook Lee, Ali Harakeh, and Steven L. Waslander. 2018. Joint 3D Proposal Generation and Object Detection from View Aggregation. In *2018 IEEE/RSJ International Conference on Intelligent Robots and Systems (IROS)*. 1–8.
- [16] Alex H. Lang, Sourabh Vora, Holger Caesar, Lubing Zhou, Jiong Yang, and Oscar Beijbom. 2019. PointPillars: Fast Encoders for Object Detection From Point Clouds. In *2019 IEEE/CVF Conference on Computer Vision and Pattern Recognition (CVPR)*. 12689–12697.
- [17] Jiale Li, Shujie Luo, Ziqi Zhu, Hang Dai, Andrey S Krylov, Yong Ding, and Ling Shao. 2020. 3D IoU-Net: IoU guided 3D object detector for point clouds. *arXiv preprint arXiv:2004.04962* (2020).
- [18] Jiale Li, Yu Sun, Shujie Luo, Ziqi Zhu, Hang Dai, Andrey S Krylov, Yong Ding, and Ling Shao. 2021. P2V-RCNN: Point to Voxel Feature Learning for 3D Object Detection from Point Clouds. *IEEE Access* (2021).
- [19] P. Li, X. Chen, and S. Shen. 2019. Stereo R-CNN Based 3D Object Detection for Autonomous Driving. In *2019 IEEE/CVF Conference on Computer Vision and Pattern Recognition (CVPR)*. 7636–7644.
- [20] Ming Liang, Bin Yang, Yun Chen, Rui Hu, and Raquel Urtasun. 2019. Multi-Task Multi-Sensor Fusion for 3D Object Detection. In *2019 IEEE/CVF Conference on Computer Vision and Pattern Recognition (CVPR)*. 7337–7345.
- [21] Ming Liang, Bin Yang, Shenlong Wang, and Raquel Urtasun. 2018. Deep Continuous Fusion for Multi-sensor 3D Object Detection. In *European Conference on Computer Vision (ECCV)*. 641–656.
- [22] Tsung-Yi Lin, Priya Goyal, Ross B. Girshick, Kaiming He, and Piotr Dollár. 2020. Focal Loss for Dense Object Detection. *IEEE Transactions on Pattern Analysis and Machine Intelligence* 42, 2 (2020), 318–327.
- [23] Xinhai Liu, Zhizhong Han, Xin Wen, Yu-Shen Liu, and Matthias Zwicker. 2019. L2G Auto-encoder: Understanding Point Clouds by Local-to-Global Reconstruction with Hierarchical Self-Attention. In *MM '19: The 27th ACM International Conference on Multimedia*. ACM, 989–997.
- [24] Zhe Liu, Xin Zhao, Tengting Huang, Ruolan Hu, Yu Zhou, and Xiang Bai. 2020. TANet: Robust 3D Object Detection from Point Clouds with Triple Attention. In *2020 AAAI Conference on Artificial Intelligence (AAAI)*. 11677–11684.
- [25] Ilya Loshchilov and Frank Hutter. 2017. Fixing Weight Decay Regularization in Adam. *CoRR* abs/1711.05101 (2017). arXiv:1711.05101
- [26] Shujie Luo, Hang Dai, Ling Shao, and Yong Ding. 2020. C4AV: Learning Cross-Modal Representations from Transformers. In *European Conference on Computer Vision (ECCV)*. Springer, 33–38.
- [27] Shujie Luo, Hang Dai, Ling Shao, and Yong Ding. 2021. M3DSSD: Monocular 3D single stage object detector. In *IEEE/CVF Conference on Computer Vision and Pattern Recognition (CVPR)*. 6145–6154.
- [28] Charles R. Qi, Wei Liu, Chenxia Wu, Hao Su, and Leonidas J. Guibas. 2018. Frustum PointNets for 3D Object Detection from RGB-D Data. In *2018 IEEE/CVF Conference on Computer Vision and Pattern Recognition (CVPR)*. 918–927.
- [29] Charles Ruizhongtai Qi, Hao Su, Kaichun Mo, and Leonidas J. Guibas. 2017. PointNet: Deep Learning on Point Sets for 3D Classification and Segmentation. In *2017 IEEE Conference on Computer Vision and Pattern Recognition (CVPR)*. 77–85.
- [30] Charles Ruizhongtai Qi, Li Yi, Hao Su, and Leonidas J. Guibas. 2017. PointNet++: Deep Hierarchical Feature Learning on Point Sets in a Metric Space. In *Conference on Neural Information Processing Systems (NeurIPS)*. 5099–5108.
- [31] Shaoqing Ren, Kaiming He, Ross B. Girshick, and Jian Sun. 2017. Faster R-CNN: Towards Real-Time Object Detection with Region Proposal Networks. *IEEE Transactions on Pattern Analysis and Machine Intelligence* 39, 6 (2017), 1137–1149.
- [32] Olaf Ronneberger, Philipp Fischer, and Thomas Brox. 2015. U-Net: Convolutional Networks for Biomedical Image Segmentation. In *2015 Medical Image Computing and Computer-Assisted Intervention (MICCAI)*, Vol. 9351. 234–241.
- [33] Shaoshuai Shi, Chaoxu Guo, Li Jiang, Zhe Wang, Jianping Shi, Xiaogang Wang, and Hongsheng Li. 2020. PV-RCNN: Point-Voxel Feature Set Abstraction for 3D Object Detection. In *2020 IEEE/CVF Conference on Computer Vision and Pattern Recognition (CVPR)*. 10526–10535.
- [34] Shaoshuai Shi, Xiaogang Wang, and Hongsheng Li. 2019. PointRCNN: 3D Object Proposal Generation and Detection From Point Cloud. In *2019 IEEE/CVF Conference on Computer Vision and Pattern Recognition (CVPR)*. 770–779.
- [35] Shaoshuai Shi, Zhe Wang, Jianping Shi, Xiaogang Wang, and Hongsheng Li. 2020. From Points to Parts: 3D Object Detection from Point Cloud with Part-aware and Part-aggregation Network. *IEEE Transactions on Pattern Analysis and Machine Intelligence* (2020), 1–1.
- [36] Weijing Shi and Raj Rajkumar. 2020. Point-GNN: Graph Neural Network for 3D Object Detection in a Point Cloud. In *2020 IEEE/CVF Conference on Computer Vision and Pattern Recognition (CVPR)*. 1708–1716.
- [37] Leslie N. Smith and Nicholas Topin. 2019. Super-convergence: Very fast training of neural networks using large learning rates. In *Artificial Intelligence and Machine Learning for Multi-Domain Operations Applications*, Vol. 11006. 1100612.
- [38] Pei Sun, Henrik Kretzschmar, Xerxes Dotiwalla, Aurelien Chouard, Vijaysai Patnaik, Paul Tsui, James Guo, Yin Zhou, Yuning Chai, Benjamin Caine, Vijay Vasudevan, Wei Han, Jiquan Ngiam, Hang Zhao, Aleksei Timofeev, Scott Ettinger, Maxim Krivokon, Amy Gao, Aditya Joshi, Yu Zhang, Jonathon Shlens, Zhiheng Chen, and Dragomir Anguelov. 2020. Scalability in Perception for Autonomous Driving: Waymo Open Dataset. In *2020 IEEE/CVF Conference on Computer Vision and Pattern Recognition (CVPR)*. 2443–2451.
- [39] Sourabh Vora, Alex H. Lang, Bassam Helou, and Oscar Beijbom. 2020. PointPainting: Sequential Fusion for 3D Object Detection. In *2020 IEEE/CVF Conference on Computer Vision and Pattern Recognition (CVPR)*. 4603–4611.
- [40] Yue Wang, Alireza Fathi, Abhijit Kundu, David A. Ross, Caroline Pantofaru, Thomas A. Funkhouser, and Justin Solomon. 2020. Pillar-Based Object Detection for Autonomous Driving. In *European Conference on Computer Vision (ECCV)*, Vol. 12367. Springer, 18–34.
- [41] Yizhou Wang, Yen-Ting Huang, and Jenq-Neng Hwang. 2019. Monocular Visual Object 3D Localization in Road Scenes. In *MM '19: The 27th ACM International Conference on Multimedia*. ACM, 917–925.
- [42] Z. Wang, H. Fu, L. Wang, L. Xiao, and B. Dai. 2019. SCNet: Subdivision Coding Network for Object Detection Based on 3D Point Cloud. *IEEE Access* 7 (2019), 120449–120462.
- [43] Zonghan Wu, Shirui Pan, Fengwen Chen, Guodong Long, Chengqi Zhang, and Philip S. Yu. 2020. A Comprehensive Survey on Graph Neural Networks. *IEEE Transactions on Neural Networks and Learning Systems* (2020), 1–21.
- [44] L. Xie, C. Xiang, Z. Yu, G. Xu, Z. Yang, D. Cai, and X. He. 2020. PI-RCNN: An Efficient Multi-Sensor 3D Object Detector with Point-Based Attentive Cont-Conv Fusion Module. In *2020 AAAI Conference on Artificial Intelligence (AAAI)*. 12460–12467.
- [45] Yan Yan, Yuxing Mao, and Bo Li. 2018. SECOND: Sparsely Embedded Convolutional Detection. *Sensors* 18, 10 (2018), 3337–3354.
- [46] Zetong Yang, Yanan Sun, Shu Liu, and Jiaya Jia. 2020. 3DSSD: Point-Based 3D Single Stage Object Detector. In *2020 IEEE/CVF Conference on Computer Vision and Pattern Recognition (CVPR)*. 11037–11045.
- [47] Zetong Yang, Yanan Sun, Shu Liu, Xiaoyong Shen, and Jiaya Jia. 2019. STD: Sparse-to-Dense 3D Object Detector for Point Cloud. In *2019 IEEE/CVF International Conference on Computer Vision (ICCV)*. 1951–1960.

- [48] Dingfu Zhou, Jin Fang, Xibin Song, Liu Liu, Junbo Yin, Yuchao Dai, Hongdong Li, and Ruigang Yang. 2020. Joint 3D Instance Segmentation and Object Detection for Autonomous Driving. In *2020 IEEE/CVF Conference on Computer Vision and Pattern Recognition (CVPR)*. 1836–1846.
- [49] Yin Zhou, Pei Sun, Yu Zhang, Dragomir Anguelov, Jiyang Gao, Tom Ouyang, James Guo, Jiquan Ngiam, and Vijay Vasudevan. 2019. End-to-End Multi-View Fusion for 3D Object Detection in LiDAR Point Clouds. In *2019 Annual Conference on Robot Learning (CoRL)*, Vol. 100. 923–932.
- [50] Yin Zhou and Oncel Tuzel. 2018. VoxelNet: End-to-End Learning for Point Cloud Based 3D Object Detection. In *2018 IEEE/CVF Conference on Computer Vision and Pattern Recognition (CVPR)*. 4490–4499.